Supporting Information

On the Origin of Low Energy d-d Excitations Observed on Wet-Chemically Prepared Cobalt Bearing Nanoparticles by *2p3d* Resonant X-ray Emission Spectroscopy

Matti M. van Schooneveld,*,† Amélie Juhin,† Carlos Campos-Cuerva,† Thorsten Schmitt,‡ and Frank M.F. de Groot*,†

† Inorganic Chemistry and Catalysis, Debye Institute for Nanomaterials Science, Utrecht University, Universiteitsweg 99, 3584 CG Utrecht, The Netherlands

‡ Swiss Light Source, Paul Scherrer Institut (PSI), CH-5232 Villigen PSI, Switzerland

Table of contents

EXPERIMENTAL SECTION

Materials: nickel(II) acetylacetonate ($Ni(acac)_2$; 95%), trioctylphosphine oxide (TOPO; 99%), dioctyl ether (99%), 1,2-dichlorobenzene (anhydrous, 99%), 2-propanol (anhydrous, 99%), and cyclohexane (anhydrous, 99.5%) were purchased from Sigma-Aldrich. Dicobalt octacarbonyl ($Co_2(CO)_8$; hexane stabilized, 95%), oleic acid (OA; 97%), and acetone (anhydrous, 99.8%) were obtained from Acros Organics. Nitric acid (pro analysis, 65%), hydrochloric acid (fuming, 37%), and hydrogen peroxide (stabilized, for synthesis, 30%) were obtained from Merck. Sulfuric acid (>95%) was obtained from Fischer Chemical. All chemicals were used as received.

ε-Co nanoparticle synthesis: the ε-Co and nanoparticles were prepared following Puntes et al.[19] 0.45 g (1.32 mmol) $Co_2(CO)_8$ was dissolved in 3 mL anhydrous 1,2-dichlorobezene in an airtight flask. In a separate airtight flask 0.10 g (0.26 mmol) TOPO and 0.18 g (0.64 mmol) OA were dissolved in 2 mL dry 1,2-dichlorobezene. The metal precursor and ligand solutions were prepared under magnetic stirring inside a nitrogen-atmosphere glove box (H_2O/O_2 levels <2 ppm). In a nitrogen-atmosphere Schlenk line outside the glove box, a three-neck round bottom flask was evacuated and flushed with N_2 gas three times. Subsequently, 10 mL of dry 1,2-dichlorobezene was injected into the flask through a septum and heated until reflux temperature (186 °C; boiling point 1,2-dichlorobezene). Next, the 2 mL OA- and TOPO-containing solvent and the metal precursor solution were injected, in this order, from airtight vials in the hot 1,2-dichlorobezene. Upon injection the metal precursor solution changed instantaneously from yellow to black. Mixtures were refluxed for 30 min, allowed to cool to room temperature, and transferred back to the glove box before further analysis.

$Co_{0.65}Ni_{0.35}$ nanoparticle synthesis: the $Co_{0.65}Ni_{0.35}$ alloy nanoparticles were synthesized through our recently reported acetonated cobalt carbonyl method.[20] In short, 0.40 g (1.17 mmol) $Co_2(CO)_8$ and 0.30 g (1.17 mmol) $Ni(acac)_2$ were left to dissolve for 30 min in 3 mL of anhydrous acetone in a nitrogen-atmosphere glove box, under occasional stirring of the flask by hand. Next, 0.30 g (1.06 mmol) OA and 0.18 g (0.47 mmol) TOPO were simultaneously added to 12 mL anhydrous dioctyl ether in a synthesis flask inside the glove box, and the solution was subsequently heated to 280 °C in a nitrogen Schlenk line outside the glove box. The metal precursor solution was then injected from airtight vials in the hot, ligand-containing solvent. Mixtures were refluxed for 30 min, allowed to cool to room temperature, and transferred back to the glove box before further analysis.

Note that in all the nanoparticle syntheses, glassware was cleaned with Piranha etch (3/1 v/v sulfuric acid/hydrogen peroxide), Aqua regia (3/1 v/v nitric/hydrochloric acid), excessive deionized water, and anhydrous acetone prior to use.

Nanoparticle size-selective precipitation and washing: size-selective precipitation of the magnetic ε-Co and $Co_{0.65}Ni_{0.35}$ nanoparticles was done with a 1.3 T magnet. For this purpose, typically 1 mL of an as-synthesized nanoparticle dispersion was submitted to four size-selective steps using increasing amounts of anhydrous 2-propanol as an anti-solvent (0.5, 1, 2, and 4 mL in the first, second, third and fourth step, respectively). In the first step the solution was put on the magnet to destabilize the largest nanoparticles. The sediment was kept and re-dissolved in 1 mL of anhydrous cyclohexane for further analysis. To the supernatant the extra amount of 2-propanol was added and the mixture was put on the magnet again. This was repeated until four size-selected batches were obtained in 1 mL of cyclohexane. From these batches a dispersion was chosen with the desired average nanoparticle size (by TEM analysis). The chosen batch was subsequently washed three times. To this end the nanoparticles, dissolved in cyclohexane, were all destabilized with 2-propanol. The supernatant was removed and the sediment re-dispersed in cyclohexane, after which the cycle was repeated.

Transmission electron microscopy (TEM), energy dispersive X-ray spectroscopy (EDX), and X-ray powder diffraction (XRD) characterization: The obtained nanoparticles were characterized by TEM, EDX and XRD prior to the *2p* XAS and *2p3d* RXES measurements. For TEM, carbon-coated formvar Cu-grids (200 mesh; Agar Scientific) were dipped in nanoparticle dispersions and imaged on a Tecnai 12 (FEI) operating at 120 kV, equipped with a SIS CCD camera Megaview II. ITEM software (Olympus) was used to measure size distributions based on at least 200 particles. A Tecnai 20 (FEI) microscope operated at 200 kV, equipped with a field emission gun, Gatan 694 camera, and EDAX spectrometer, was used for EDX-analysis. For this purpose the washed and size-selective precipitated samples were used. At least 5 different micron-sized spots and up to 20 individual nanoparticles were analyzed to determine particle composition and to test its uniformity over the batch.

XRD diffraction patterns were acquired on a Bruker D8 advance diffractometer. Cobalt $K\alpha_{1,2}$ X-ray tubes (λ=1.790 Å) operating at 30 kV were used, with currents of 45 and 10 mA, respectively. Typically, data points were acquired between $40^\circ<2\theta<110^\circ$ every 0.2° with 13 s $step^{-1}$. XRD samples were prepared inside the glove box and enclosed in an airtight and X-ray transparent holder in order to probe the non-oxidized, as prepared metal nanoparticles. The airtight XRD specimen holder with dome-like X-ray transparent cap for environmentally sensitive materials (A100B33; sample reception 25 mm diameter, 1 mm depth) was obtained from Bruker AXS.

2p XAS and 2p3d RXES spectra acquisition: For these measurements the following materials and tools were obtained. p-Type Boron-doped silicon (100)(111) surface terminated wafers (525 μm thick; cut in 7x7 mm squares; resistivity ~ 5 Ωcm) were obtained from CrysTec GmbH. Hydrofluoric acid (pro analysis, 48-51%) was obtained from Acros Organics. Plastic

tweezers (style KR) were obtained from Rubis Switzerland. Sticky carbon tape was obtained from NEM Nisshin Em.Co.Ltd. Silver epoxy paste (E4110 kit) was obtained from Epoxy Technology.

The nanoparticle dispersions were dripped onto silicon wafers inside a helium-glove box for the XAS and RXES measurements. Prior to this the silicon substrates were treated to remove oxygen species from the wafer surface and to passivate the silicon wafers with atomic hydrogen. The wafers were immersed in acetone, 2-propanol and in deionized water, respectively, and given an ultrasonic treatment for 10 minutes each. The substrates were then etched, following Thorton and Williams,[21] for 10 min with a 1/5/4 v/v/v solution of HF/ethanol/water. Subsequently, the wafers were rinsed with deionized water to remove physisorbed surfaces species,[22] before drop casting the nanoparticle solutions on the wafers. The nanoparticles were then transferred to the load-lock chamber of the beamline under exclusion of air. To this end we developed a transfer tool for atmosphere-sensitive samples into the RXES endstation in-house.

Transfer tool for XAS/RXES measurements of atmosphere-sensitive samples

A dedicated tool for the transfer of atmosphere-sensitive samples into the RXES endstation at the ADRESS beamline was developed in-house. A schematic representation of the tool and the way it is employed is given in reference 18. The tool consists of 5 parts: (1) an aluminum bottom part (10x23x27 mm) on top of which the sample is deposited. This part also contains a screw thread for sample transfer purposes into the endstation. (2) An O-ring (20 mm diameter), that is used between (1) and (3&4) which is an aluminum cylinder (14 mm diameter) consisting of two separate pieces. In between (3) and (4), part (5) a 4 mm thick septum is clamped. The usage of the transfer tool is as follows. It can be loaded in an inert environment, in this study inside a helium-atmosphere glove box. The samples, here the air-sensitive metal nanoparticles, can be mounted on part (1) of the tool. Subsequently, part (2) till (5) can be mounted together and placed over the sample on part (1). Through part (5), the septum in the top part, the pressure in the void between the bottom and top part can be reduced by sucking out atmosphere with a syringe. The top and bottom part are now sucked tightly onto each other. The tool is subsequently transferred to and mounted in the load lock chamber of the beamline. By pumping down the chamber, the reduced pressure in the void of the tool rapidly becomes an overpressure and the top part pops off. This allows the final sample transfer into the measurement chamber of the beamline (here at ~10^{-8} mbar) without the sample having been exposed to air.

COMPUTATIONAL SECTION

Density functional theory (DFT): The ORCA software package was used for all DFT[25,26] calculations. Molecular geometries were first optimized using the BP86 functional[27,28] and Ahlrichs split valence plus polarization (SVP),[29] and auxiliary SV/J for Coulomb fitting, basis set implemented in ORCA from the TurboMole basis set library under ftp.chemie.uni-karlsruhe.de/pub/jbasen. The self-consistent field (SCF) energy convergences were performed using Direct Inversion in Iterative Subspace (DIIS) for all structures with two or less transition metal atoms. For clusters containing more such atoms Kollmar's DIIS (KDIIS) was used alternatively. A second round of geometry optimization was in all cases performed unless mentioned otherwise. This was done using the optimized structure of the first cycle with the BP86 functional and a default-2 triple-zeta valence plus polarization (def2-TZVP) basis set.[30,31] For transition metal containing complexes spin unrestricted SCF calculations were applied with a slow (SlowConv) and tight (TightSCF) convergence, setting the tolerances for the last energy change to $1x10^{-8}$ Ha and the last maximum density change to $1x10^{-7}$ Ha. The tolerances for geometry optimization were $5x10^{-6}$ Ha for the last energy change, $1x10^{-4}$ ($2x10^{-3}$) Ha for the last root mean square gradient (step) and $3x10^{-4}$ ($4x10^{-3}$) Ha for the last maximum gradient (step). All geometries optimized without problem and no Hartree-Fock (HF) spin contaminations were found.

For all calculations the charge and spin multiplicity of the species were varied in order to find the most stable species. In order to identify the most stable structural isomer of the adsorbates, different starting configurations of clusters were used in the DFT geometry optimization calculations. The start configurations were identified by calculating all stable configurations with the MM2 force field method in the Chem3D Pro software. As an example in Supporting Figure S1 it is shown how the stable binding geometry of acetate molecules on small cobalt clusters (6 and 10 atoms) was found. The molecular orbitals (MO's) obtained by the calculations were examined by Mulliken orbital population analyses to allow for an atomic orbital interpretation of the MO's.

Time-dependent DFT (TD-DFT): A BP86 functional, a TZVP basis set and slow (SlowConv) and tight (TighSCF) convergence were used. The resolution of identity (RI) and Tamm-Dancoff approximation (TDA) that are applied by default in ORCA were switched off. The fractional occupation number was switched on for the unrestricted spin open shell systems in order to prevent symmetry breaking of degenerate orbitals. The first 25 transitions were by standard obtained in the TD-DFT calculations. The tolerance in the convergence of energies of the excited states was $1x10^{-8}$ Ha and the convergence of the norm of the residual vectors was $1x10^{-8}$ Ha. It was checked on model compounds such as $Co^{2+}(H_2O)_6$ that the followed approach yielded excitations (≤ 1 eV) in agreement with experimental optical absorption data.

Ligand field multiplet (LFM) calculations. *2p* XAS and *2p3d* RXES spectra were simulated using the freeware multiplet program available under the name Charge Transfer Multiplet for XAS (CTM4XAS).[38] The splitting of d-levels due to atomic effects are calculated using a HF code that includes relativistic effects as developed by Cowan.[39,40] This generates the atomic multiplets or atomic manifolds. The further splitting of atomic multiplets in a ligand field and/or due to charge transfer (CT) effects can subsequently be calculated in CTM4XAS using the Butler-Thole codes.[41] For the current calculations only the ligand field effects were included, since CT effects modify the *2p* XAS and *2p3d* RXES spectra of Co^{II} only little.[15] In such cases we consider the omission of CT effects in the calculations to be favorable. The values of the applied electronic structure parameters used in the interpretation are summarized in Table 1 of the main text.

LFM calculations for XAS. For our calculations we approximate cobalt to have a formal Co^{II} valence in models **A** and **B** (see the Results section for explanation of the models). Co^{II} can be described effectively by a $2p^63d^7$ ground state configuration. For simulation of the *2p* XAS spectra all electric dipole-allowed electron transitions from the ground state to a $2p^53d^8$ excited state are calculated, together with their oscillator strengths. To this end, the ground state and intermediate state energy levels are first calculated.

The atomic multiplets in the ground state depend mainly on the 3d-3d direct Coulomb interactions and 3d spin-orbit coupling ζ_{3d}. The intermediate state is in addition affected by 2p-3d direct Coulomb and Coulomb exchange interactions and 2p spin-orbit coupling ζ_{2p}. The 3d-3d direct Coulomb and 2p-3d direct Coulomb and Coulomb exchange interactions can be described by two-electron integrals, called the Slater or Slater-Condon integrals. The radial parts of these integrals are obtained *ab initio* within the HF limit for a given electron configuration by the program. The program also automatically scales the values to 80% of their original HF values to correct for intra-atomic configuration interaction and hybridization effects. The radial parts of the integrals that define the 3d-3d direct Coulomb interactions are F^2_{dd} and F^4_{dd} and are given in Table 1. In an analogous way the 2p-3d direct Coulomb interactions are set by F^2_{pd} and the 2p-3d Coulomb exchange interactions by G^1_{pd} and G^3_{pd}. Next to the direct Coulomb and Coulomb exchange interactions the program calculates the 2p and 3p spin-orbit coupling values within the HF limit, but it does not scale the original values further down.

The user can modify the obtained atomic parameters in order to correct for effects not included in the Hamiltonian. Here we have further reduced both the values of the radial parts of the Slater integrals and the value of the 3d spin-orbit coupling. The radial parts of the Slater integrals (F^2_{dd}, F^4_{dd}, F^2_{pd}, G^1_{pd} and G^3_{pd}) were not further scaled in model **A** and all scaled to 95% in model **B** (this corresponds to 80% and 76% of the HF values). Reduction of the Slater integrals of the free metal ion is often done in LFM calculations to effectively describe the delocalization of 3d electrons on to ligands. This d-

electron delocalization is also known as the nephelauxetic effect.[44] In fact, F^2_{dd} and F^4_{dd} are related to the Racah parameters B and C through relations given by Cowan[40]: $B=(9F^2_{dd} - 5F^4_{dd})/441$ and $C=5F^4_{dd}/63$. For models **A** and **B** the Racah parameter B in the ground/excited state is 0.124/0.118 eV and 0.132/0.126 eV, respectively. For Racah parameter C the ground/excited state value is 0.458/0.435 eV and 0.489/0.465 eV, respectively. This implies that in model **A** the d-electrons are slightly more localized on the metal ion. Furthermore, the value of ζ_{3d} was reduced here to 50% and 75% of its atomic HF value in models **A** and **B**. The reason for such reductions was discussed previously for Co^{II} in CoO on page 11 of Van Schooneveld et al.[24]

Once the atomic multiplets are calculated, a further splitting or branching of these states occurs in the ligand field. Here the D_{4h} point group symmetry is used to simulate the effect of the carboxylate ligands. In D_{4h} the ligand field is described by the parameters 10Dq, Ds and Dt.[10] The values of 10Dq, Ds and Dt are given in Table 1.

The transitions that are calculated between the ground and excited, ligand-field-affected, atomic states yield absolute intensities. These intensities of the discrete transitions are convoluted with a Lorentzian function $\Gamma 2p_{3/2}$ to account for the $2p_{3/2}$ core hole lifetime broadening at the $2p_{3/2}$ XAS edge. A second convolution of the allowed transitions is done with a Gaussian function G (fwhm) to account for the instrumental broadening. Note that the calculations do not yield absolute energy positions and the resulting spectra are shifted in energy for comparison with the experimental spectra. All XAS spectra were calculated at a temperature of 17 °C (290 K).

LFM calculations for 2p3d RXES. The inelastic scattering function $F(\Omega,\omega)$ is described by the resonant term of the Kramers-Heisenberg formula[42,43] that defines the interference between the X-ray induced electron excitation and subsequent decay processes:

$$F(\Omega,\omega) = \sum_f \left| \sum_i \frac{< f \mid T_2 \mid i >< i \mid T_1 \mid g >}{E_g + \hbar\Omega - E_i + \mathrm{i}\Gamma_i} \right|^2 \times \frac{\Gamma_f / 2\pi}{(E_g + \hbar\Omega - E_f - \hbar\omega)^2 + {\Gamma_f}^2/4}$$

where $|g>$, $|i>$ and $|f>$ indicate the ground, intermediate and final state configuration of the probed matter and E_g, E_i, E_f are the energies. Here $\hbar\Omega$ and $\hbar\omega$ are the energies of the incident and emitted photon. T_1 and T_2 are operators describing the radiative transitions by absorbed and emitted photons and are electric dipole in nature for the *2p3d* RXES transitions. Γ_i gives the spectral Lorentzian broadening due to the finite time of the core-hole existence in the intermediate state. The second term implies that energy should be conserved in the overall RXES process and that a further Lorentzian broadening Γ_f occurs due the finite life time of the hole in the final state.

The LFM simulations of the *2p3d* RXES spectra for Co^{II} are done using the $g=2p^63d^7$ ~~i~~$=2p^53d^8$ ~~f~~$=2p^63d^8\underline{d}$ transitions. Although the final state $2p^63d^8\underline{d}$ configuration is formally equal to $2p^63d^7$ we use this notation to indicate that the final state still can have a hole in the 3d band. Only in an elastic scattering event, where $\hbar\Omega = \hbar\omega$, the final state configuration has no 3d hole (other than the initial three 3d holes). Lorentzian functions accounting for the intermediate ($\Gamma 2p_{3/2}$) and final ($\Gamma 3d$) state lifetime of the hole were used to convolute the allowed RXES transitions. Gaussian functions accounting for monochromator- and spectrometer-induced experimental broadening were applied to convolute the spectra further. Note that for models **A** and **B** the fwhm of the Gaussians was 0.1 and 0.2 eV, respectively, in order to mimic the different experimental resolutions. All RXES calculations took the interference effects between the X-ray absorption and emission into account. The shown RXES calculations were all done for the ground state, which formally relates to a situation at -273.15 °C (zero K). In Supporting Figure S4 calculations are shown that take the Boltzmann-distributed population of excited states at 17 °C (290 K) into account for model **A**. Although excited states are accessible at room temperature these do not affect the spectra significantly and the same was shown for model **B**'s calculations previously.[15] All spectra were calculated with the transition probabilities that correspond to the used LH polarization in the experiment (as discussed in the spectral acquisition part). Therefore the parallel or σ contribution of the light was taken incident on the sample together with the perpendicular or π contribution being detected (in the multiplet program this corresponds to "parallel" incident light plus outgoing "left" light summed with "parallel" incident plus outgoing "right" light).

LFM multiplet symmetry labeling: the different states of the initial state configuration $2p^63d^7$ have been labeled in Figures 4c and 5 in D_{4h} symmetry without 3d spin-orbit coupling using the following method: in spherical symmetry without 3d spin-orbit coupling the energy level degeneracies, Tanabe-Sugano linear formulas and Hund's rules were used to assign symmetry labels. An octahedral ligand field O_h was introduced subsequently. For Figure 4c (model **A**) 10Dq was set to -0.2 eV at once, for Figure 5 (model **B**) 10Dq was raised in steps of 0.3 eV. A tetragonal distortion D_{4h} was then introduced. For model **A** two steps were followed in which in step 1 Ds and in step 2 Dt were set to their values given in Table 1. For model **B** three steps were performed in which Ds was increased each time by 0.05 eV. Finally a 3d spin-orbit coupling was applied in steps of 25% of its atomic HF values until the final value for both models. During the introduction of these parameters the states were systematically tracked and the results were in agreement with the tables in Griffith.

RESULTS

DFT geometry optimization

Thermodynamic DFT calculations revealed that a total spin multiplicity (M_s=2S+1) of 4 for single cobalt species and of 7 for dicobalt species yield the most stable bonds with carboxylates. For larger clusters the optimum spin multiplicity is not easily predicted and alternatively it was set to 1 for all calculations shown in Supporting Figure S1. On the left side of the Figure different geometric start configurations, indicated with numbers, are given for an $OOC_2H_3^-$ species on different clusters. On the right side the BP86 SVP SV/J optimized geometries are given with the same numbers and their final state energies in Hartree. In Figure 2a seven out of eight tested configurations converge to a bond where the acetate has both of its two oxygen atoms atop one cobalt atom. One metastable structural isomer, number *4*, is identified. In Figure S1b seven out of eight configurations had the acetate attached to two cobalt atoms through two oxygen atoms. One metastable structural isomer, number ***6***, is identified. In Figure S1c both configurations give the acetate bonding to the cobalt cluster through two oxygen atoms. From these calculations we conclude that each of the two oxygen atoms in the carboxylate functional group resides atop one cobalt atom each in the most likely mode of bonding.

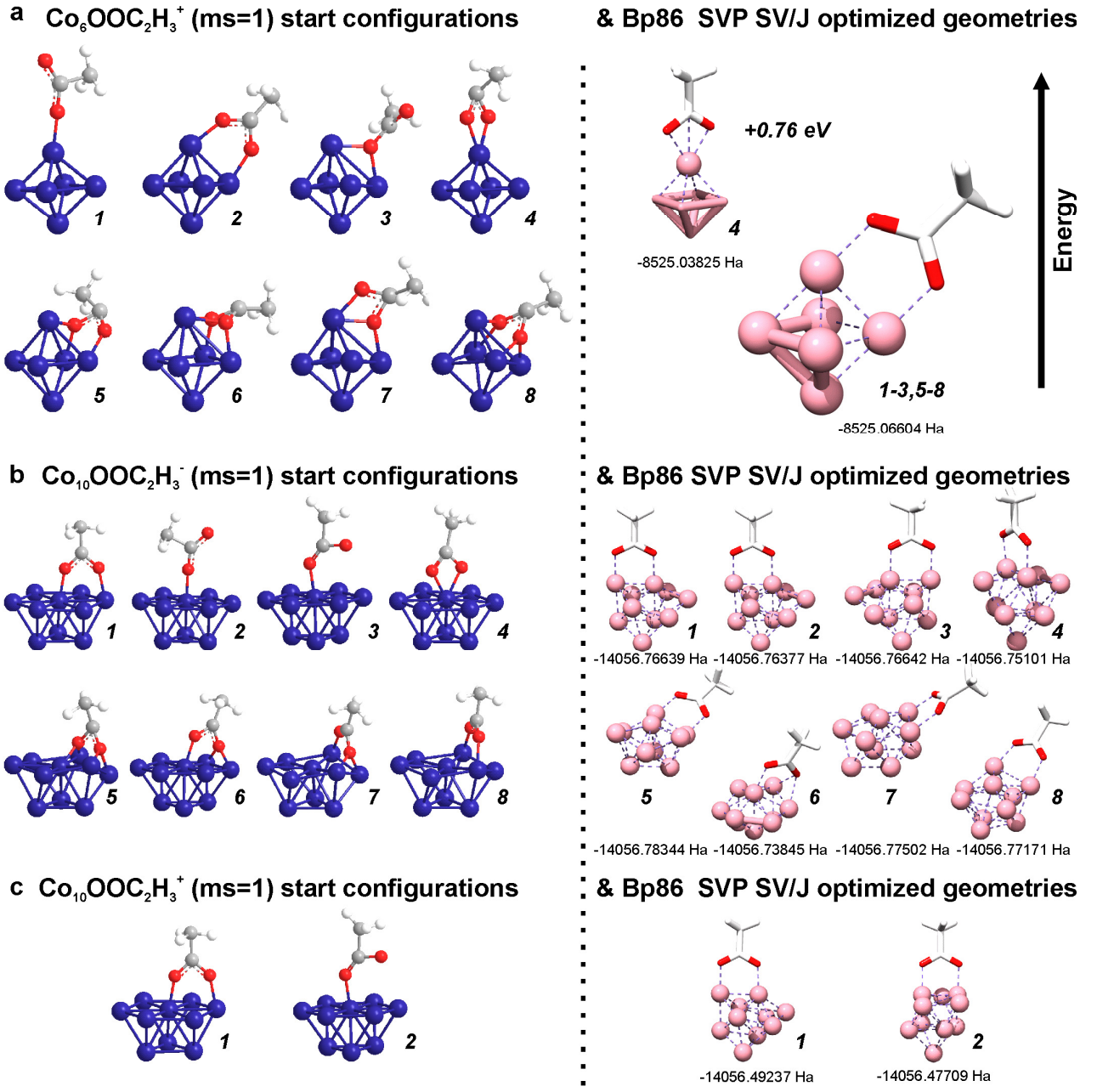

Figure S1. Determination of the stable acetate ligand geometry on top of small cobalt clusters by DFT calculations. Optimization of $OOC_2H_3^-$ on (a) a Co_6^{2+}, (b) a Co_{10} cluster and (c) a Co_{10}^{2+} cluster.

Charge and structure effects on the TD-DFT transitions

Figure S2 shows the effects of the number of metal entities in a cluster, the metal valency and the metal-oxygen-carbon bond angle on TD-DFT transitions. Increasing the number of metal atoms in a metal-ligated cluster increases the number of inter-metal and total TD-DFT transitions strongly. This renders the use of TD-DFT in the prediction of RXES transitions troublesome for multi-metallic species since inter-metal transitions are not seen in RXES spectra (they are detected by UV/Vis, but RXES from a formal metal shows only X-ray fluorescence). Therefore a one-metal approximation is used in the main text. When Co^{2+} is replaced by Co^{0} in the TD-DFT calculations shown in Figure 4b of the main text, less and shifted TD-DFT transitions are found. Cobalt(0) methanolate has three transitions below 1 eV. Next to the fixed bond angle of 120° used in the TD-DFT of the main text for cobalt(II) methanolate (that mimics the 116° bond angle in the dicobalt carboxylate bond) two relaxed geometries for cobalt(II) methanolate and trimethylphosphine oxide were obtained with different basis sets (SVP and Def2-TZVP). These yield bond angles as indicated in the Figure. The transitions shift to slightly lower energies for smaller values of the bond angle, especially in case of the cobalt(II) trimethylphosphine oxide.

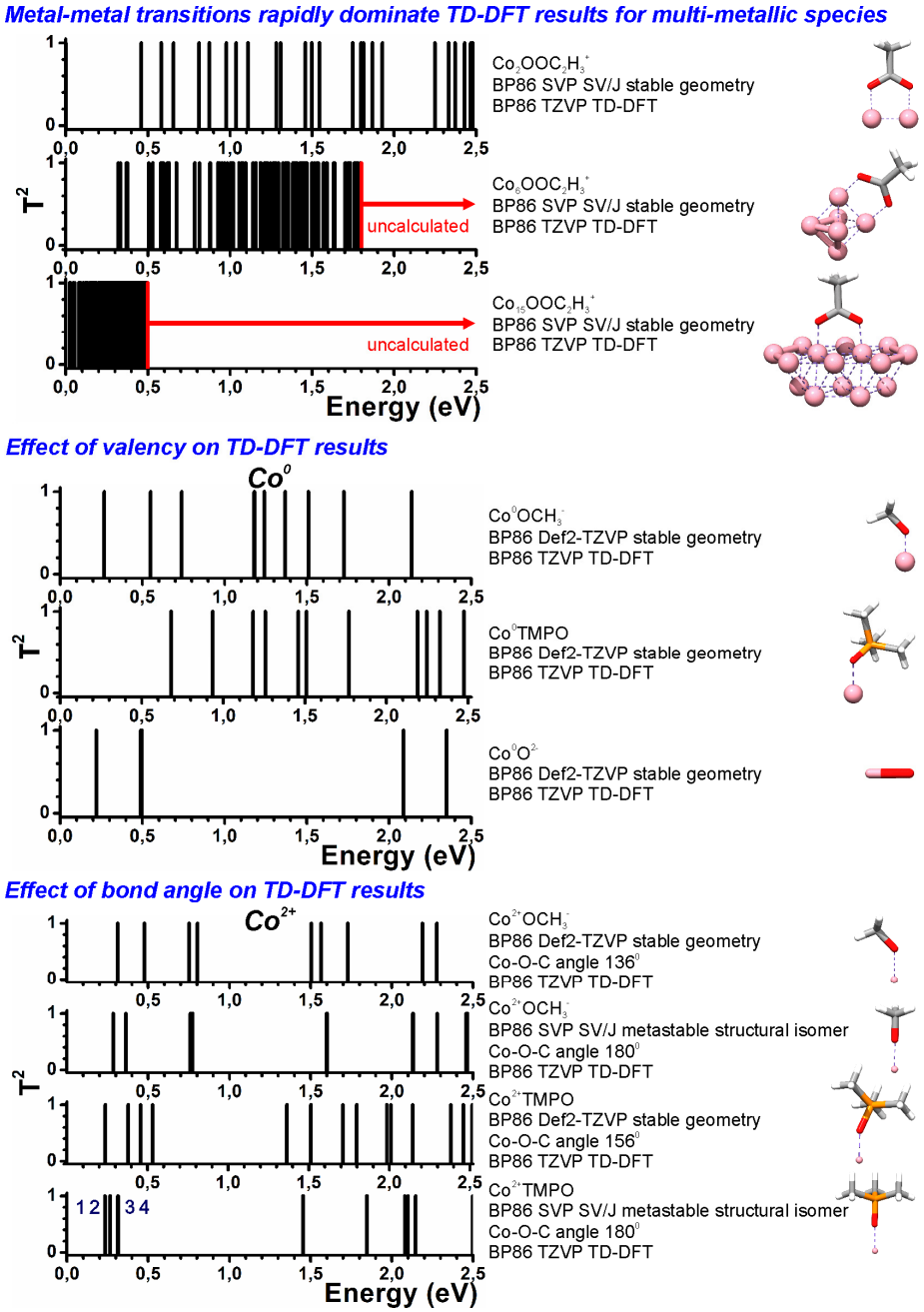

Figure S2. Effects of the number of metal entities in a cluster, the metal valence and the metal-oxygen-carbon bond angle on TD-DFT transitions.

Prediction of LFM parameters in model A

In the main text a cobalt(II) methanolate species with a Co-O-C bond angle mimicking that of dicobalt carboxylate (~120°) is used in TD-DFT calculations. Here we first discuss the differences and similarities between this bond and a cobalt(II)cobalt(0) acetate bond. Then we discuss how this can be used to provide restrictions for the LFM calculations.

Considering that only neutral reactants were used in the synthesis, the formation of [cobalt(II)$_2$-oleate]$^{3+}$ bonds is unlikely. On the basis of this, the cobalt oleate interactions are mimicked here with cobalt(II)cobalt(0)-oleate bonds, although charge conservation requires a compensating electron, possibly through attachment of another oleate to neutral cobalt atoms.

Given this choice, the cobalt(II)cobalt(0)-oleate bond spin-down populated MO's involving the 3d cobalt atomic orbitals are given in Supporting Figure S3. All corresponding spin-up populated 3d-rich MO's are fully occupied and do not participate in excitations between 3d-rich MO's. The atomic orbital contributions to the MO's, obtained from Mulliken population analyses, are also shown. The main difference between the cobalt(II)cobalt(0)-oleate and the cobalt(II) methanolate bond (with the 120° Co-O-C bond) is that in the former the $3d_{x^2-y^2}$ orbitals lie lower in energy than the $3d_{xy}$ orbitals. In the cobalt(II) methanolate species both orbitals are in principal degenerate, but depending on the interaction with the methyl hydrogen atoms (which are absent in the acetate) the $3d_{x^2-y^2}/3d_{xy}$ orbitals are found to be each half of the times possessing the lowest energy when geometry optimization from random start configuration is performed. In both the cobalt(II)cobalt(0)-oleate and the cobalt(II) methanolate bond, cobalt $3d_{yz}$ forms bonding and anti-bonding MO's with oxygen $2p_y$ and cobalt $3d_{xz}$ is partly hybridized with $3d_{z^2}$ to form a bonding and anti-bonding configuration with a hybrid of oxygen $2p_x$ and $2p_z$. Although the cobalt $3d_{yz}$-based MO's in this bond actually have higher energy than the $3d_{xz}$-based MO's, we assume for simplicity that the states are degenerate to allow for a prediction of the ligand field parameters in D_{4h} symmetry.

The above leads to an average 3d atomic orbital distribution as shown on the upper right side of Supporting Figure S3. This sequence of orbitals yields the prediction that the numerical value of 10Dq should be negative. The origin of the TD-DFT transitions is shown as a function of the main atomic orbital constituents that make up the MO's between which the transitions occur. Here $3d_{x^2-y^2} \rightarrow 3d_{xy}$ means a transition from $3d_{xy,x^2-y^2}$ to $3d_{xy}$.

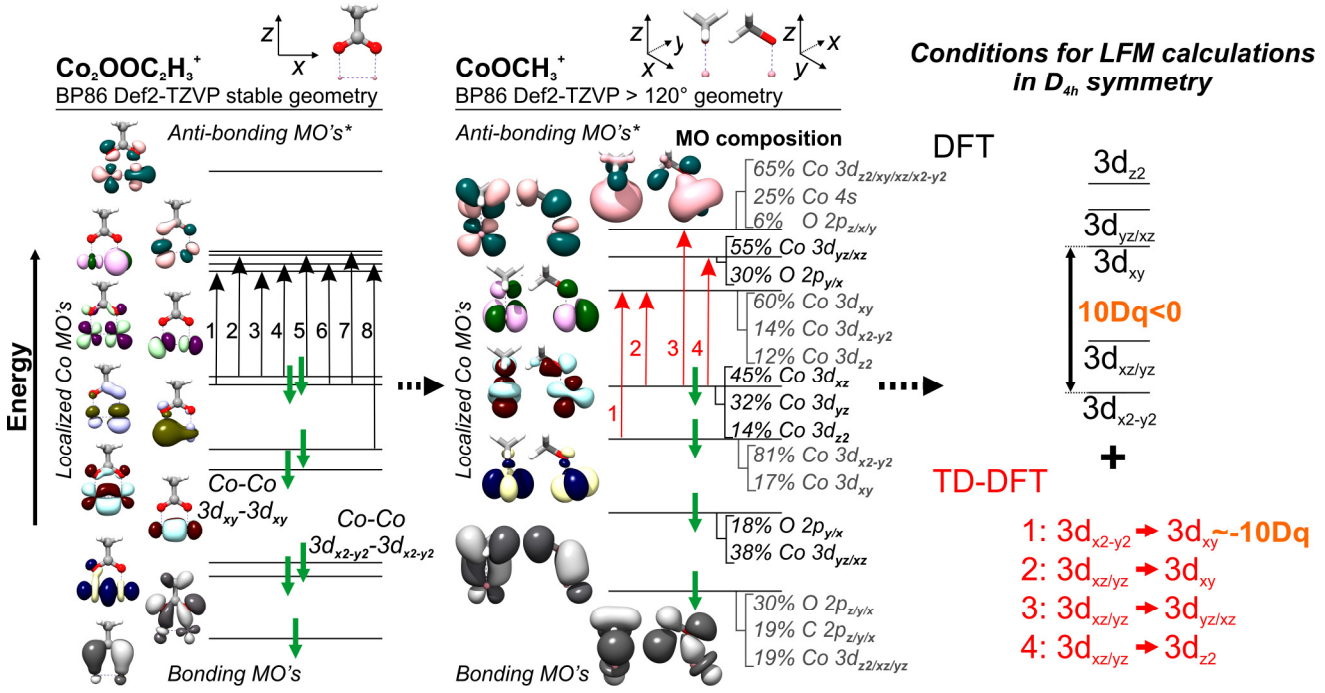

Figure S3. Spin-down populated MO's and Mulliken population analyses for the cobalt(II)cobalt(0) acetate (left) and cobalt(II) methanolate bond (middle) and restrictions for ligand field parameters within D_{4h} symmetry. The MO electron occupation is shown with green thick arrows. The TD-DFT transitions are indicated with thin black (acetate) or red (methanolate) numbered arrows. The red numbers in the middle panel correspond to the transitions as shown in Figure 4b of the main text. On the right, splitting of the 3d atomic orbitals in the bond is approximated in a tetragonal D_{4h} point group symmetry.

LFM RXES temperature effects on model A

In Figure S4 LFM calculations at excitation energy *d* are shown that take the Boltzmann-distributed population of excited states at 17 °C (290 K) into account for model **A**. Although two excited states are significantly populated at room temperature, the Boltzmann-weighted spectrum does not possess a spectral shape that is significantly different from the ground state spectrum. The LFM calculations allow not for the calculation of other temperature effects than the Boltzmann population of excited states. We previously discussed this in detail and refer the interested reader to the discussion in reference 15 for more details.

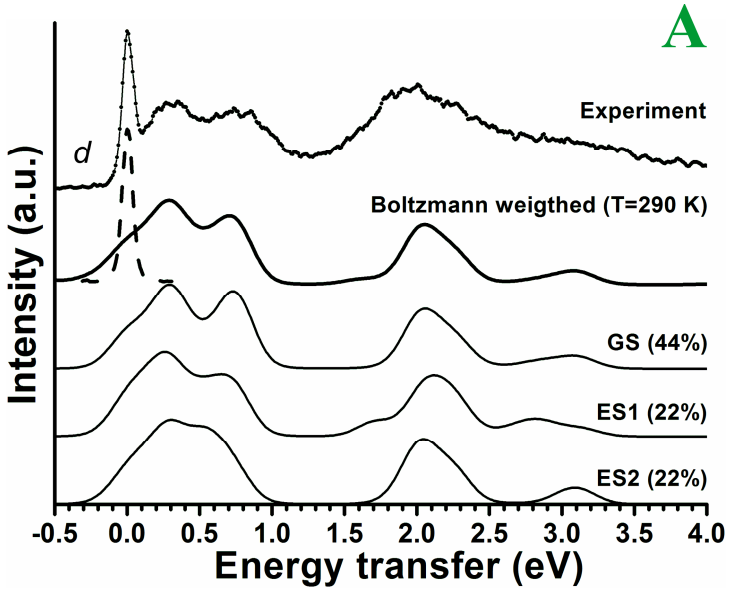

Figure S4. Experimental *2p3d* cobalt RXES spectrum (black dots+line) of the $Co_{0.65}Ni_{0.35}$ nanoparticles acquired at excitation energy *d*, together with the LFM spectra (solid lines) of the ground state (GS), first and second excited states (ES1 and ES2). Their spectral weight at 290 K is indicated in parenthesis. The Boltzmann weighted spectrum is shown together with a black dashed spectrum at 0 eV that was taken off the sample to reveal background X-ray scattering.

DISCUSSION

Fraction of surface atoms in nanoparticles

The fraction of atoms in the surface of the ε-Co nanoparticles with a 5.0 and 8.4 nm diameter as well as in the surface of the 3.6 nm $Co_{0.65}Ni_{0.35}$ nanoparticles is estimated. We use $V_{shell}/V_{total}=(r^3-(r-D)^3)/r^3$ where V_{shell} and V_{total} are the volumes of a spherical nanoparticle shell and the total spherical nanoparticle, r is the average radius of the nanoparticles and D is the thickness of the shell. For D one can hypothetically use an average Co-Co distance in the ε-Co unit cell of 0.25 nm.[63] For the $Co_{0.65}Ni_{0.35}$ nanoparticle an equal metal-to-metal distance of 0.25 nm is used from the fcc Co unit cell.[64] This gives an atomic surface fraction of 19%, 14% and 9% for particles with a 3.6, 5.0 and 8.4 nm diameter, respectively. For the $Co_{0.65}Ni_{0.35}$ particles one can assume that the Co:Ni ratio in the surface is identical to the bulk. However, recently we discussed that in our particles the surface is likely fully covered by cobalt. This further increases the percentage of cobalt in the surface to a maximum of ~40%.

REFERENCES

The complete references of (13-14), (17), (50-54), (56) and (65) are:

(13) Ghiringhelli, G.; Piazzalunga, A.; Dallera, C.; Trezzi, G.; Braicovich, L.; Schmitt, T.; Strocov, V. N.; Betemps, R.; Patthey, L.; Wang, X.; Grioni, M. SAXES, a High Resolution Spectrometer for Resonant X-Ray Emission in the 400–1600 eV Energy Range. *Rev. Sci. Instrum.* **2006**, *77*, 113108.

(14) Strocov, V. N.; Schmitt, T.; Flechsig, U.; Schmidt, T.; Imhof, A.; Chen, Q.; Raabe, J.; Betemps, R.; Zimoch, D.; Krempasky, J.; Wang, X.; Grioni, M.; Piazzalunga, A.; Patthey, L. High-Resolution Soft X-ray Beamline ADRESS at the Swiss Light Source for Resonant Inelastic X-ray Scattering and Angle-Resolved Photoelectron Spectroscopies. *J. Synchrotron Radiat.* **2010**, *17*, 631-643.

(17) *In general this holds for substrates that do not show resonant Raman features, but only X-ray fluorescence.*

(50) *Alternatively, such peaks may result from non-core hole related, additional excitations that are present in the intermediate state, for example charge transfer, and are maintained after decay to the RXES final state configuration..*

(51) *Note that the spectra taken at the beginning of the $2p_{3/2}$ XAS edge shows decay to low-energy excitations, while the spectrum acquired at excitation energy e has about the same intensity for low-energy excitations and excitations above 2 eV. One reason for this is that the first spectrum decays through a high-spin $2p^5 3d^8$ intermediate state and the second through a mixed high-spin low-spin $2p^5 3d^8$ intermediate state.*

(52) *We interpret this to be a result of an electron delocalization process in the intermediate 2p3d RXES state that is faster than the filling of the 2p core hole by a localized d-electron.*

(53) *We use the spectroscopic convention to put the initial state at the right side of a transition.*

(54) Liu, H.; Guo, J.; Yin, Y.; Augustsson, A.; Dong, C.; Nordgren, J.; Chang, C.; Alivisatos, P.; Thornton, G.; Ogletree, D. F.; Requejo, F. G.; de Groot, F.; Salmeron, M. Electronic Structure of Cobalt Nanocrystals Suspended in Liquid. *Nano Lett.* **2007**, *7*, 1919-1922.

(56) *We note however that a limited number of other studies exist that have used DFT calculations to obtain input parameters for LFM models,[56-59] and that developments on more rigorous ab initio multiplet models exist.[60-62]*

(65) Respaud, M.; Broto, J. M.; Rakoto, H.; Fert, A. R.; Thomas, L.; Barbara, B.; Verelst, M.; Snoeck, E.; Lecante, P.; Mosset, A.; Osuna, J.; Ely, T. O.; Amiens, C.; Chaudret, B. Surface Effects on the Magnetic Properties of Ultrafine Cobalt Particles. *Phys. Rev. B* **1998**, *57*, 2925-2935.